Chapter 5 *Electrochemical Studies of Dy Doped α-MnO$_2$ Nanorods for Supercapacitor Application*

5.1 Introduction

Incorporation of dopants in MnO$_2$ lattice offer a possibility to tune the electrochemical properties as α-MnO$_2$ possesses tunnel cavity of as large as 0.46 nm where dopants can easily be inducted. It has been reported in literatures that dopants such as Ni^{2+}, Cu^{2+}, Co^{2+}, Fe^{3+}, Cr^{3+}, Mo^{6+}, V^{5+}, W^{6+}, etc. have been doped in MnO$_2$ lattice and exhibit a significant increase in specific capacitance as the surface area and porosity of the lattice grow [36], [129], [130], [197]. It is critical to note that the porosity and surface area of the material also increases by doping rare earth element in α-MnO$_2$, which ultimately controls the specific capacitance. For example, Lanthanum doped MnO$_2$ nanoneedles and cerium doped MnO$_2$ nanoflowers are used to modulate the porosity of the MnO$_2$ nanostructures and exhibit a specific capacitance of 479.38 Fg^{-1} and 514.38 Fg^{-1}, respectively, at a scan rate of 10Vs^{-1} in 1M Li$_2$SO$_4$ electrolyte compared to the pure MnO$_2$ having specific capacitance of 466.28 Fg^{-1}[198]. However, no studies have been reported on the electrochemical properties of Dy doped MnO$_2$. In this chapter, we have undertaken the studies on pseudo-capacitive performance of Dy doped α-MnO$_2$ nanorods to use as an electrode material for a pseodocapacitor.

In this chapter, we have synthesised different mol concentration of Dy doped α-MnO$_2$ nanorods by simple one step hydrothermal technique. The structural and microstructural

properties analysed by XRD, Raman spectroscopy, SEM, and TEM are discussed in section 5.2. Surface area and pore size analysis from Nitrogen adsorption desorption data are discussed in section 5.3. α-MnO$_2$: Dy (15 mol %) electrode facilitates mass transport, improve the electrode kinetics investigated extensively using cyclic voltammetry (CV), Galvanostatic charge/ discharge and electrochemical impedance spectroscopy (EIS) and are thoroughly discussed in section 5.4. The effect of introducing Dy in α-MnO$_2$ nanorods on its electrochemical performance has been discussed in this chapter and concluded in section 5.5.

5.2 Structural and Microstructural Analysis

5.2.1 X-ray Diffraction

Figure 5.1 depicts the X-ray diffraction patterns of as synthesised bare and Dy doped α-MnO$_2$. The observed diffraction peaks corresponding to miller indices (110), (200), (220), (310), (211), (420), (301), and (411) are well ascribed to tetragonal phase of α-MnO$_2$ (JCPDS No. 44-0141) with space group I4/m. Moreover, no other peaks related to impurity have been observed in XRD pattern confirming the formation of pure α-MnO$_2$ phase irrespective of Dy content. This indicates that Dy ions enter into the tunnel of α-MnO$_2$ without changing the structure. The intensity of diffraction peaks reflects the formation of well crystalline α-MnO$_2$ powder. The crystallinity however monotonously decreases with increasing Dy concentration up to 15 mol% followed by an increase at 20 mol%. Decrease in crystallinity with increase in Dy concentration indicates the distortion in α-MnO$_2$ lattice. The distortion causes a decrease in crystal symmetry with a reduction in interfacial energy with increasing Dy content. The distortion of lattice pertains upto 15 mol% of Dy doping in

α-MnO$_2$ lattice. Above 15 mol%, increase in the intensity of diffraction peaks signifies the limitation of incorporation of Dy ions into the tunnel of α-MnO$_2$. Thus, even increasing the doping concentration, the crystallinity does not decrease any more. Further, it is observed that diffraction peaks of α-MnO$_2$: Dy (5, 10 and 15 mol %) are much broader suggesting a systematic decrease in particle size. The decrease in crystallinity followed by an increase at 20 mol% of Dy, inhibits the incorporation of Dy ions in the tunnel of α-MnO$_2$ are examined from SEM, TEM and XPS results discussed later.
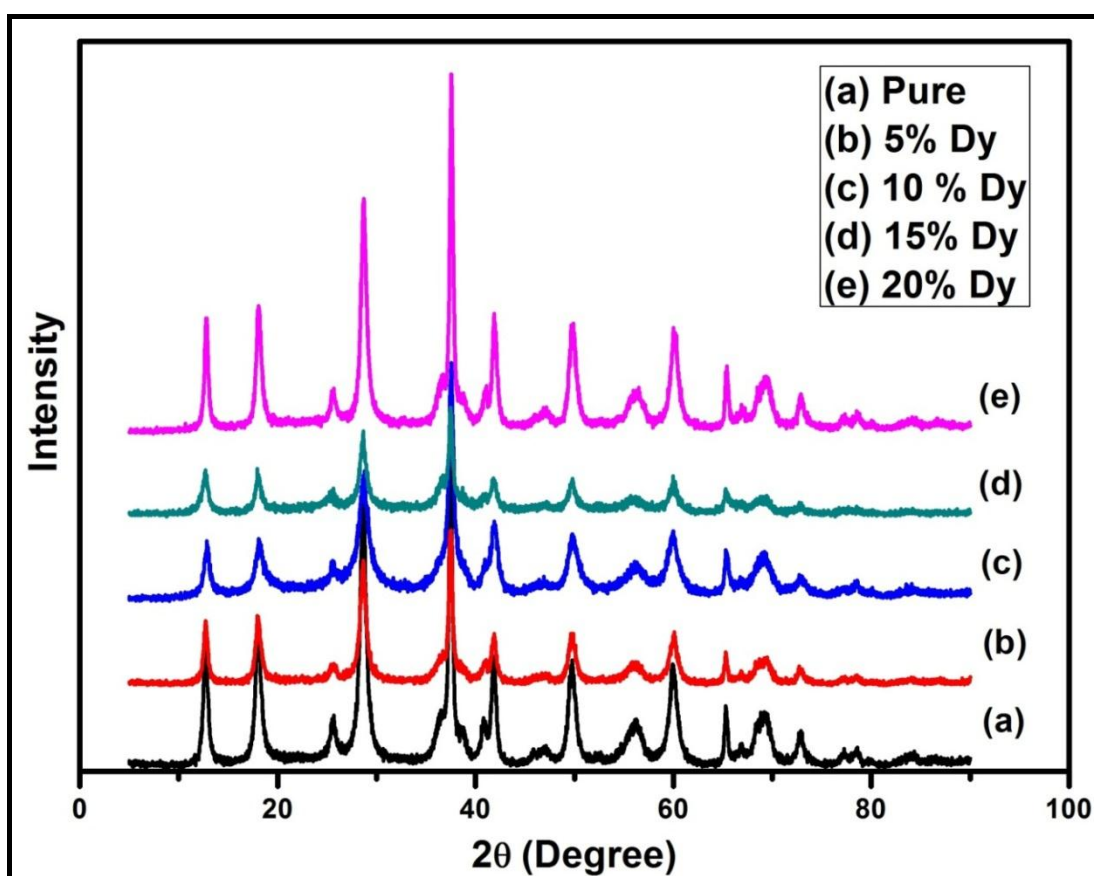

Figure 5:1 *XRD of bare α-MnO$_2$ and α-MnO$_2$: Dy (5, 10, 15, 20 mol %) nanorods.*

5.2.2 Raman Spectroscopy

Due to poor crystalline behaviour, it is difficult to apply the Rietveld refinement of the XRD data to study the changes in the structure of the material. Therefore, we have further examined the structure of above materials through Raman spectroscopy. The Raman spectra of bare and Dy doped α-MnO$_2$ are shown in figure 5.2. From the spectra of bare α-MnO$_2$, we observe two well defined strong bands of almost same intensity at 570cm^{-1} and 634 cm^{-1} corresponding to Mn-O vibrational bands. Besides, we have also observed the skeletal vibrations in between 200 to 450 cm^{-1} and deformation modes of Mn-O-Mn chain in between 450 to 550 cm^{-1}. In addition to weak bands at 183, 386, 470 and 520 cm^{-1} two sharp bands at 574 and 634 cm^{-1} have been reported by *Gao et al.* [92]. Adding 5 mol% of Dy in α-MnO$_2$, intensity of band at 634 cm^{-1} strongly enhances at the expense of former band at 570 cm^{-1}. Significant increase in the intensity of band at 634 cm^{-1} indicates the incorporation of Dy ion into the tunnel of α-MnO$_2$. Similar result has also been reported by *Tao et al.* where the doping of heavy cations like Li, Na shows significantly different intensity of above bands [155]. Further increase in Dy concentration from 5 to 15 mol%, intensity of band at 634 cm^{-1} decreases at the expense of band at 570 cm^{-1} which almost disappears. On increasing Dy concentration to 20 mol%, the intensity of the band at 634 cm^{-1} again increases with a weak band at 570 cm^{-1} as observed in low concentration sample. As the concentration of Dy increases, the peak intensity at 574 cm^{-1} decrease and suppressed significantly for α-MnO$_2$: Dy (15 mol %). This could be resulted from the increase in oxygen vacancies accompanied with Mn^{3+} ions with increase in Dy concentration. It has been reported by *Toufiq et al.* where the doping of SiO$_2$ in α-MnO$_2$ show such reduction in the intensity of Raman bands and ascribed to the decrease in the

diameter of the nanorods [174]. Combining XRD and Raman results, one may note that increase in XRD peak broadening and decrease in the intensity of Raman bands are associated with the crystallinity and microstructure of the particles which further examined through FE-SEM and BET.
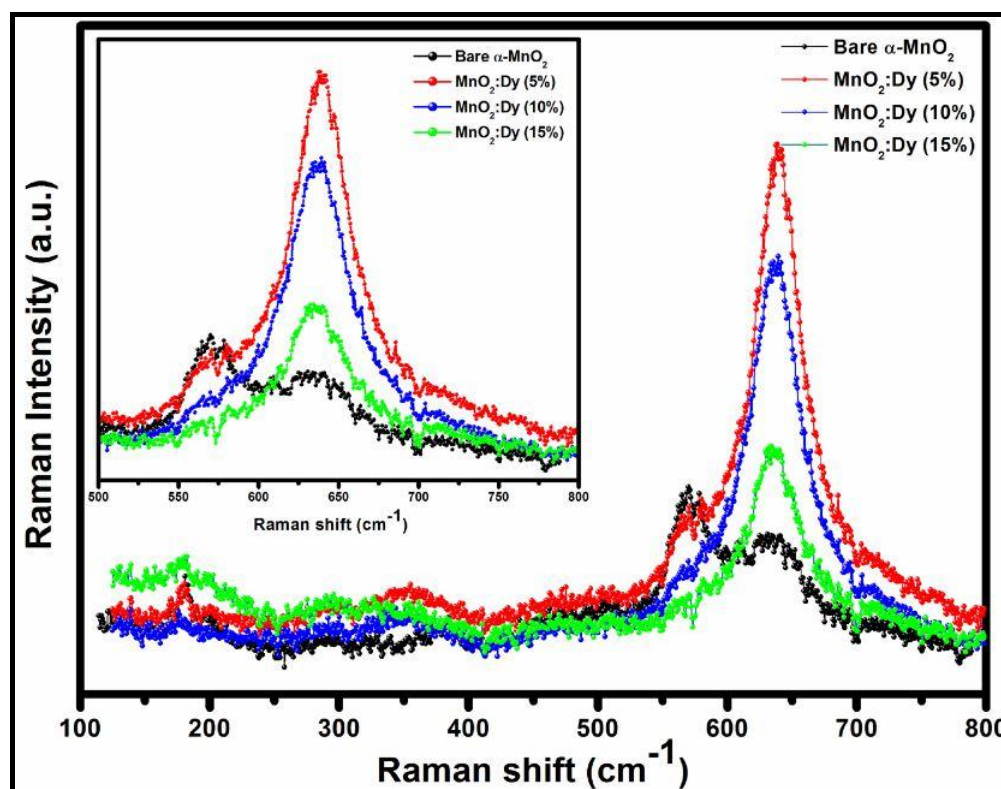

Figure 5.2: *Raman spectra of bare α-MnO₂ and α-MnO₂: Dy (5, 10, 15, 20 mol %) nanorods. Inset shows the enlarge view of Raman band at 633 cm⁻¹.*

5.2.3 Scanning Electron Microscope

Field emission scanning electron microscopy (FE-SEM) reveals the morphology of bare and Dy doped α-MnO₂ shown in Figure 5.3. (a-c). It observes that α-MnO₂ consist of nanorod like architectures with a diameter of 40 nm and an average length of 4 to 5 μm.

However, in case of α-MnO$_2$: Dy (15 mol %) micrograph we observe that diameter of nanorods decreases to 20 nm and length reduces to 70 nm which further increases to 44 nm in diameter and 4 to 5 μm in length on increasing the concentration of Dy to 20 mol% (Figure 5.4). Reduction in size of nanorods strongly indicates that incorporation of Dy inhibits the growth of nanorods upto 15mol% and allows to grow at 20 mol%. Such change in the size of the nanorods are well corroborates with decrease in crystallinity as observed from XRD. Further, we have examined the atomic percentage of Dy concentration from EDAX are tabulated in Table 5.1.
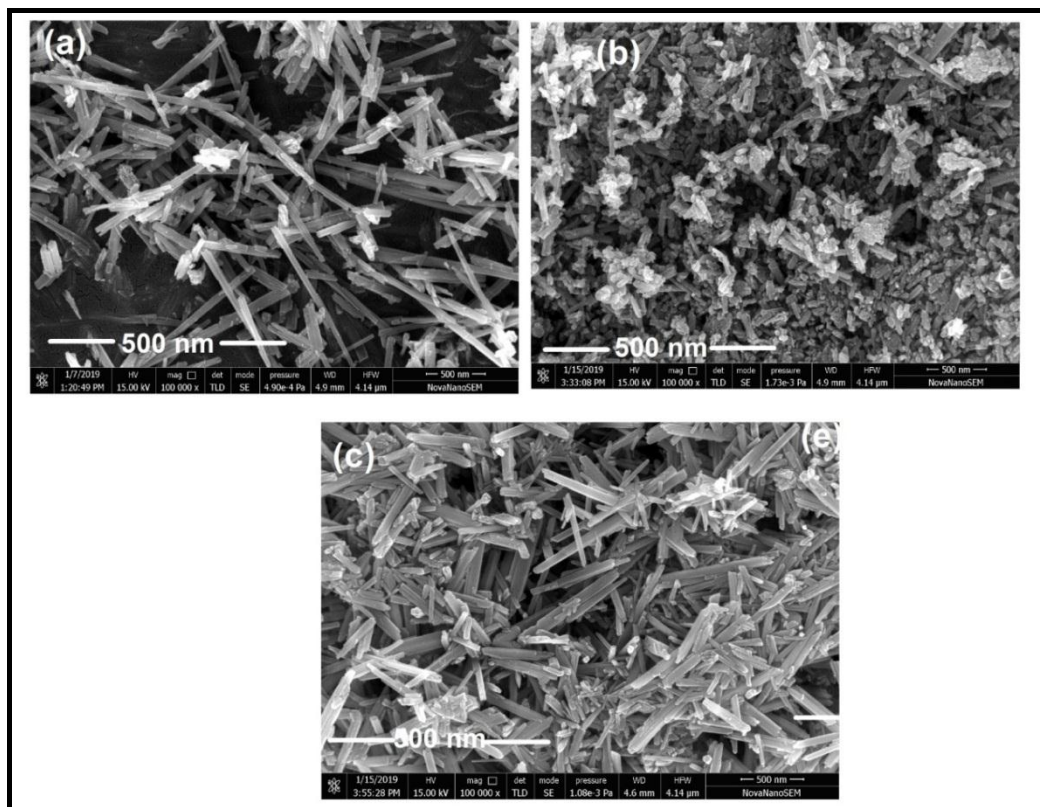
Figure 5.3: *FE-SEM images of (a) bare α-MnO$_2$, (b) α-MnO$_2$: Dy (15 mol %) (c) α-MnO$_2$: Dy (20 mol %) nanorods.*
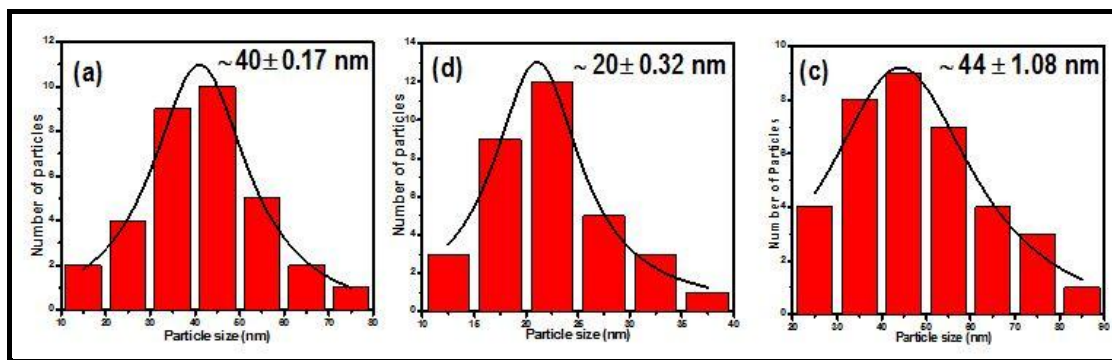
Figure 5.4: *Particle size distribution hystograms of bare α-MnO$_2$ and α-MnO$_2$: Dy (15 and 20 mol %) nanorods.*

Table 5.1: Data obtained from EDAX for Dy in α-MnO$_2$: Dy (5, 10, 15 and 20 mol %).

| Sample	Weight %	Atomic %	error
α-MnO$_2$: Dy (5 mol %)	10.54	1.94	61.02
α-MnO$_2$: Dy (10 mol %)	13.92	2.67	51.74
α-MnO$_2$: Dy (15 mol %)	11.40	2.58	36.52
α-MnO$_2$: Dy (20 mol %)	9.50	1.97	36.55

One may note that at% of Dy concentration in α-MnO$_2$:Dy (5 mol%) and α-MnO$_2$Dy: (20 mol%) are almost same which clearly confirm that 15 mol% of Dy dopant is the optimum concentration which can be incorporated into the tunnel of α-MnO$_2$ lattice.

5.2.4 Transmission Electron Microscope

To further confirm the change in aspect ratio after Dy doping, we have carried out TEM for bare and α-MnO$_2$: Dy (15 mol %) as shown in figure 5.5 (a) and (c). Aspect ratio of nanorods evaluated from particle size distribution histogram (not shown here) are found to

be 38 nm in bare α-MnO$_2$ which reduces to 12 nm after incorporating 15 mol% of Dy. HRTEM confirm the interplanar spacing (d) as 0.23 nm and 0.32 nm corresponding to (211) and (310) of tetragonal phase, I4/m of bare and α-MnO$_2$: Dy (15 mol%), respectively (see figure 5.5(b) and (d)).
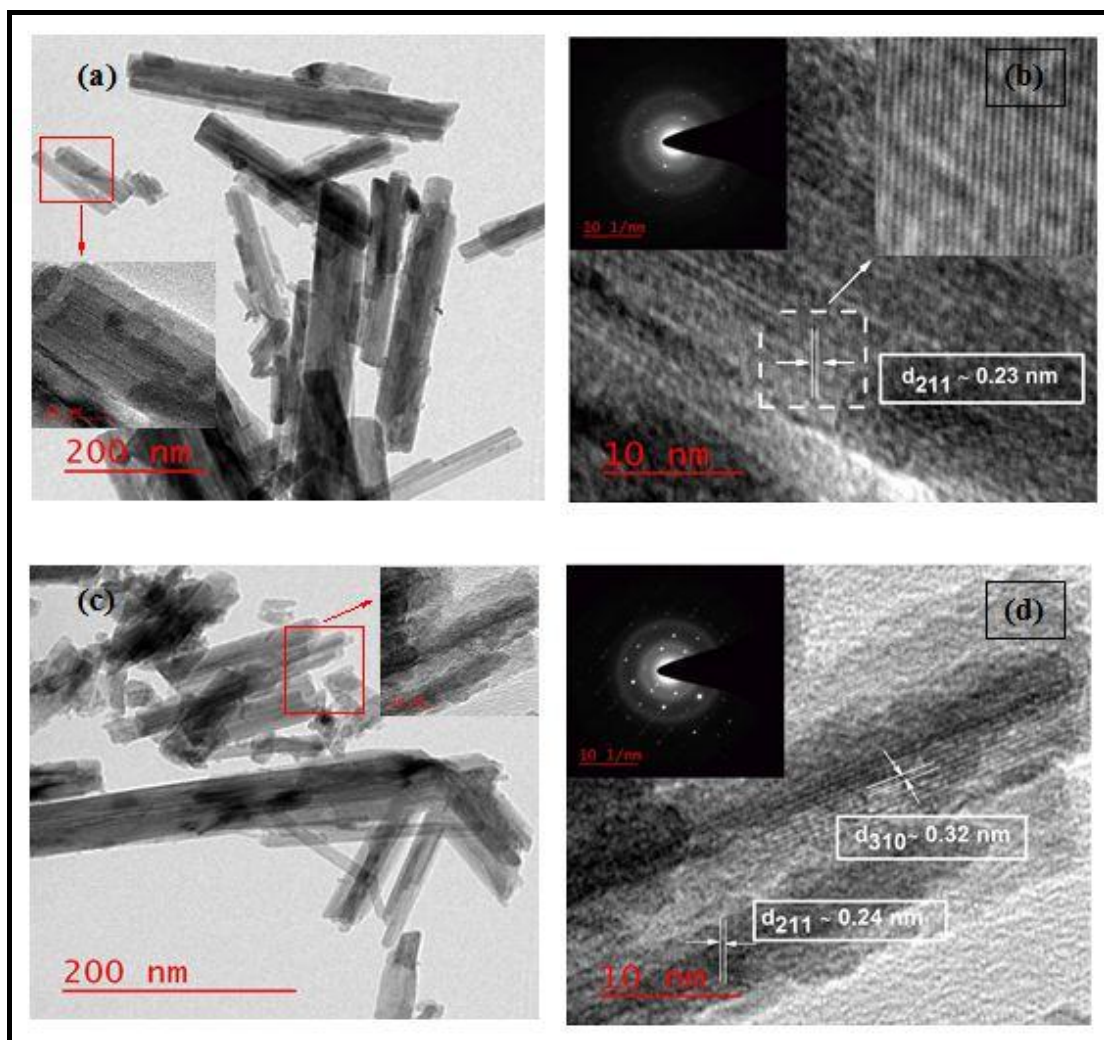

Figure 5.5: *TEM and HR-TEM images (a,b) for bare and (c, d) for α-MnO$_2$: Dy (15 mol %) nanorods. SEAD patterns are shown in the inset of (b) and (d).*

In addition, selected area electron diffraction (SAED) patterns demonstrate the coexistence of fine particles as well as crystalline nature of bare α-MnO$_2$ and α-MnO$_2$: Dy (15mol %) nanorods. However, more fine particles present in α-MnO$_2$: Dy (15mol %) than that in bare α-MnO$_2$ (Fig.5.5).

5.3 Surface Area Analysis (BET)

Reduction in the size of nanorod may effectively shorten the transport path for cation by providing large surface area which is further investigated by performing N$_2$ adsorption desorption isotherm analysis at 77K as illustrated in Figure 5.6(a). BET curves of bare α-MnO$_2$ and α-MnO$_2$: Dy (5, 10 and 15 mol %) merged at low relative pressure (P/P$_0$ < 0.4) implies a reversible adsorption and desorption process. Specific surface area of the materials is evaluated using Brunauer-Emmett-Teller (BET) adsorption isotherm which is designated as type IV with a hysteresis loop of type H3. The loop corresponding to α-MnO$_2$: Dy (15 mol %) observed at a relative pressure of 0.4 to 1 with no saturation clearly specifies the existence of mesoporous structure. It shows a steep capillary condensation in the range of 0.8-1 (P/P$_0$) signifies the formation of mesoporous morphology relative to bare α-MnO$_2$ and α-MnO$_2$: Dy (5 and 10 mol %) as framed by International Union of Pure and Applied Chemistry (IUPAC). Brunauer-Joyner-Halenda (BJH) theory is used to determine the pore size distribution shown in Figure 5.6 (b). The surface area and pore volume of bare α-MnO$_2$ is 39.66 m^{2}g^{-1} and 0.07cm^{3}g^{-1} which decrease to 16.59 m^{2}g^{-1} and 0.04 cm^{3}g^{-1} for α-MnO$_2$: Dy (5 mol %). Further increase in Dy concentration increase the surface area to 39.09 m^{2}g^{-1} and 104.48 m^{2}g^{-1} and pore volume to 0.09 cm^{3}g^{-1} and 0.21 cm^{3}g^{-1} for α-MnO$_2$: Dy (10 and 15 mol %), respectively (Table 5.2). From above results, we conclude that the incorporation of rare earth element, Dy, strongly influences the porosity of α-MnO$_2$
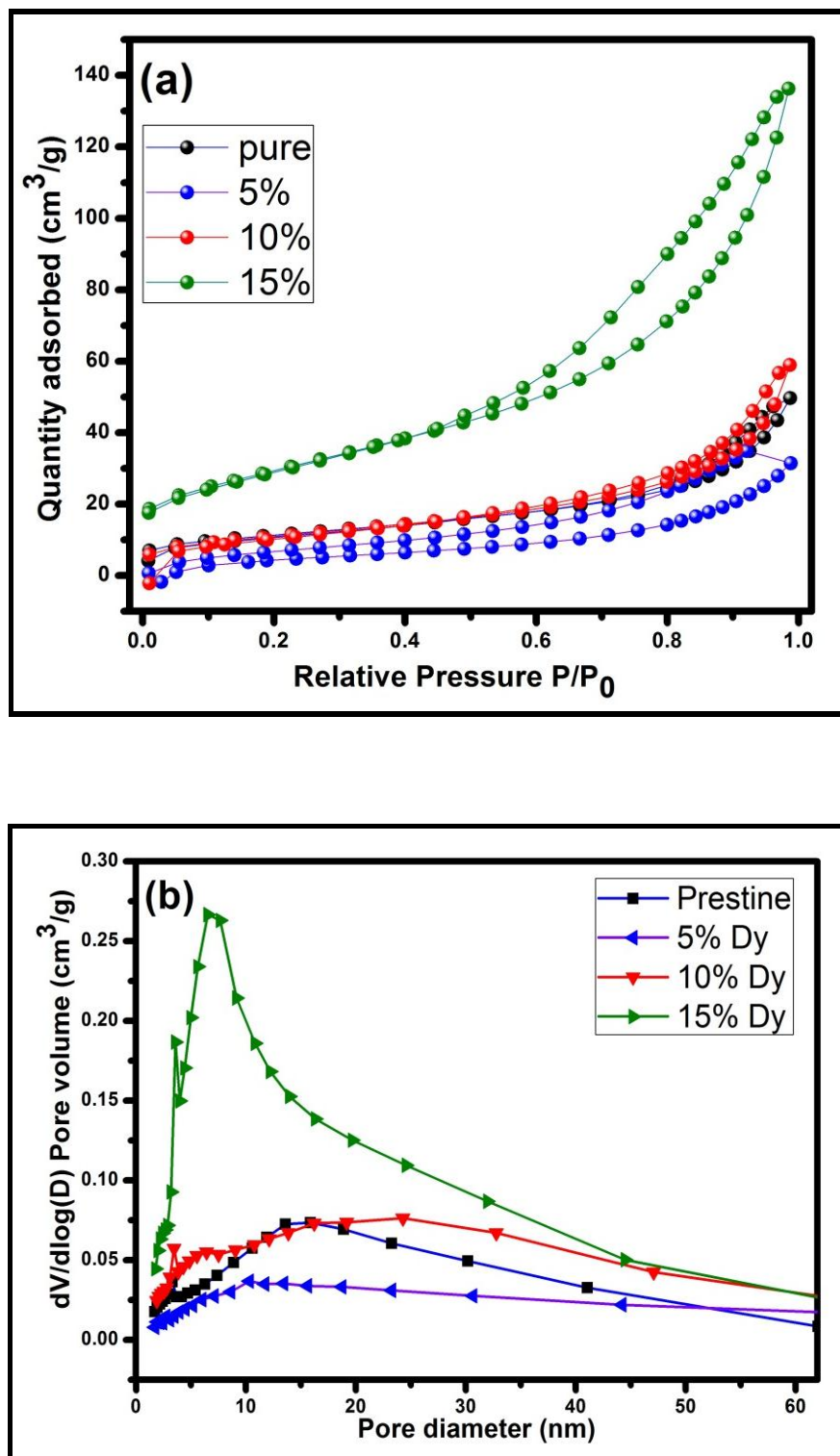
Figure 5.6: *(a) Nitrogen adsorption desorption isotherms of bare and α-MnO₂: Dy (5, 10 and 15 mol %) nanorods and (b) shows the corresponding pore size distribution.*

128

Table 5.2: Parameters obtained from Nitrogen adsorption desorption isotherm of bare and α-MnO$_2$: Dy (5, 10 and 15 mol %) nanorods.

Material	Specific surface area (m^{2}g^{-1})	Pore size (nm)	Pore volume (cm^{3}g^{-1})
MnO$_2$	39.66	7.74	0.07
MnO$_2$: Dy (5%)	16.59	7.65	0.04
MnO$_2$: Dy (10%)	39.09	9.29	0.09
MnO$_2$: Dy (15%)	104.48	8.06	0.21

nanorods. It may increase the feasibility of electron transport at the interface of electrode and electrolyte to upraise the efficiency of active material which is beneficial for an application of supercapacitor.

5.4 Electrochemical Analysis

In this section, we have investigated the effect of doping different molar concentration of Dy in α-MnO$_2$ on its electrochemical performance using cyclic voltammetry, Galvanostatic charge/discharge, and electrochemical impedance measurements, as discussed in sections 5.3.1, 5.3.2, and 5.3.3, respectively.

5.4.1 Cyclic Voltammetry

As MnO$_2$ has a large tunnel size appropriate for the intercalation of external cation with high theoretical capacitance encourage us to perform the electrochemical test to examine the effect of Dy doping on supercapacitive performance on α-MnO$_2$. Cyclic voltammetry test recorded in 1M Na$_2$SO$_4$ electrolyte over the potential range 0 to 0.8V (Vs. Ag/AgCl) at constant scan rate 5 mVs^{-1} is shown in Figure 5.7(a). Nearly rectangular CV curves specify the pseudocapacitive behaviour of electrodes exhibiting fast reversible redox reactions with

low contact resistance.   No characteristics redox peaks were observed in all electrodes indicating that over the complete voltammetric cycle charge discharge takes place at a pseudo-constant rate. Furthermore, we observe that α-MnO$_2$: Dy (15 mol %) shows largest integrated area in CV curve. As a consequence improvement in electrochemical performance by incorporating Dy ion in α-MnO$_2$ is achieved. Following equation is used to evaluate the specific capacitance from the CV curve:

$$C = \frac{\int Idv}{(m \times \Delta v \times V)} \qquad\qquad (5.1)$$

Where, I is the discharge current (A), m is the mass of active electrode material (g), Δv is the potential range of CV curve and V is the potential scan rate (mV/sec) [199][138][200]. Figure 5.7(b) shows the variation of estimated specific capacitance with different concentration of Dy at the scan rate of 5mV/sec. It is observed that the capacitance for α-MnO$_2$: Dy (15 mol %) (111 Fg^{-1}) is enhanced by twice as compared to bare α-MnO$_2$ (54 Fg^{-1}). This confirms the positive influence of Dy in pseudocapacitive performance of α-MnO$_2$ electrode. We observe high specific capacitance as compared to 0.2 mmol Ce doped α-MnO$_2$ nanorod (101.1 Fg^{-1}) at current density 1 A/g in 1M Li$_2$SO$_4$ electrolyte, V doped α-MnO$_2$ nanobelt (102 Fg^{-1}) at current density 0.5 A/g in 0.5M Na$_2$SO$_4$ electrolyte and α-MnO$_2$ nanorods (106 Fg^{-1}) at current density 4 A/g in 1M Na$_2$SO$_4$ electrolyte solution [201][89]. Hydrothermal synthesis of α-MnO$_2$ single crystal nanorod at 140˚C for 18 hr achieved a specific capacitance of 72 Fg^{-1} in 1M Na$_2$SO$_4$ electrolyte solution [30]. As α-MnO$_2$: Dy (15 mol %) show maximum background current, we further perform CV at various scan rates from 5 - 200 mV/sec as shown in figure 5.7(c). The variation in capacitance of 0, 5, 10, 15 and 20 mol % of Dy in α-MnO$_2$ electrodes with various scan rates shown in figure 5.7(d) clearly indicates an achievement of high capacitance at low

scan rate due The linear increase in maximum peak current with scan rate presented in figure 5.8 demonstrates the charge storage mechanism governed by controlled diffusion process. The maximum diffusion coefficient (α-MnO$_2$: Dy (15 mol %)) reflects fast
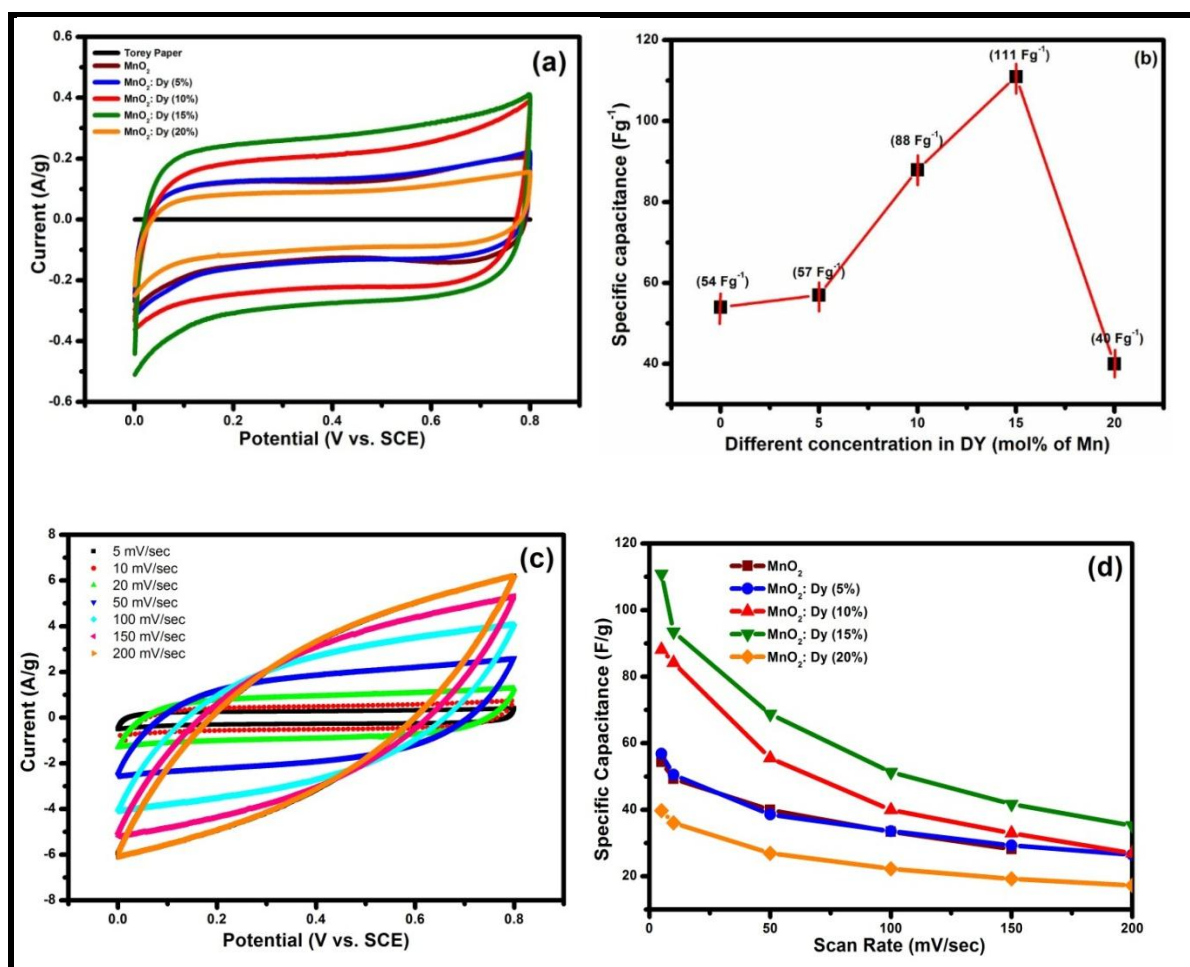
Figure 5.7: *Electrochemical performances of bare and α-MnO$_2$: Dy (5, 10, 15, 20 mol %) nanorods (a) at 5 mV/sec (b) Specific capacitance Vs. Dy concentration (c) α-MnO$_2$: Dy (15 mol %) at various scan rate and (d) specific capacitance at different scan rate.*

intercalation of large number of ions as well as reduction in electron transfer resulting high specific capacitance (111 Fg^{-1}). Such fast intercalation/deintercalation of ions in α-MnO_2: Dy (15 mol %) is due to its poor crystalline nature; generate highly porous microstructures with large surface area which facilitates the sufficient contact between electrolyte and active material and hence, shorten the transport path. In case of 20% doping of Dy ion, crystallinity suddenly increases due to presence of less amount of Dy within the tunnels which facilitates the growth rate of nanorods and limits the rate of diffusion. Along with high crystalline nature, large aspect ratio of nanorods, low concentration of oxygen vacancies are the factors responsible for the reduced capacitance in α-MnO_2: Dy (20 mol %). We have compared the highest specific capacitance obtained in α-MnO_2: Dy (15 mol %) with metal oxides reported in literatures and are presented in Table 5.3.
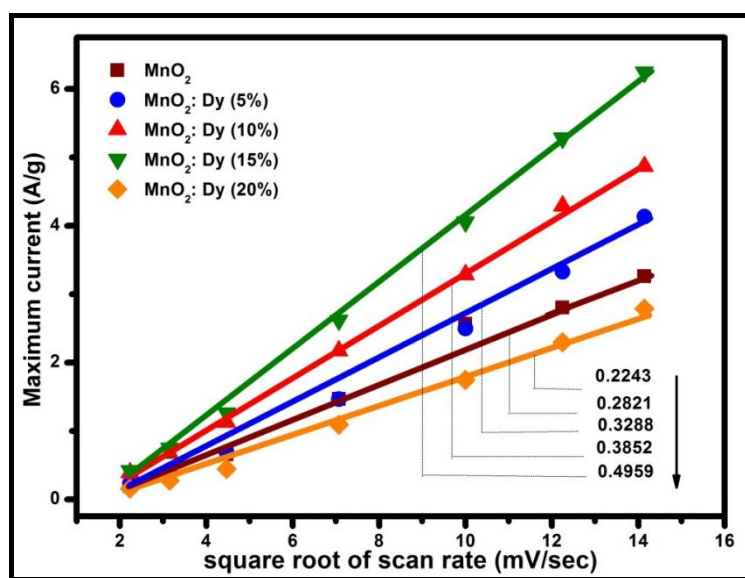
Figure 5.8: *Relationship between the maximum current and square root of the scan rate of bare and α-MnO₂: Dy (5, 10, 15, 20 mol %) nanorods.*
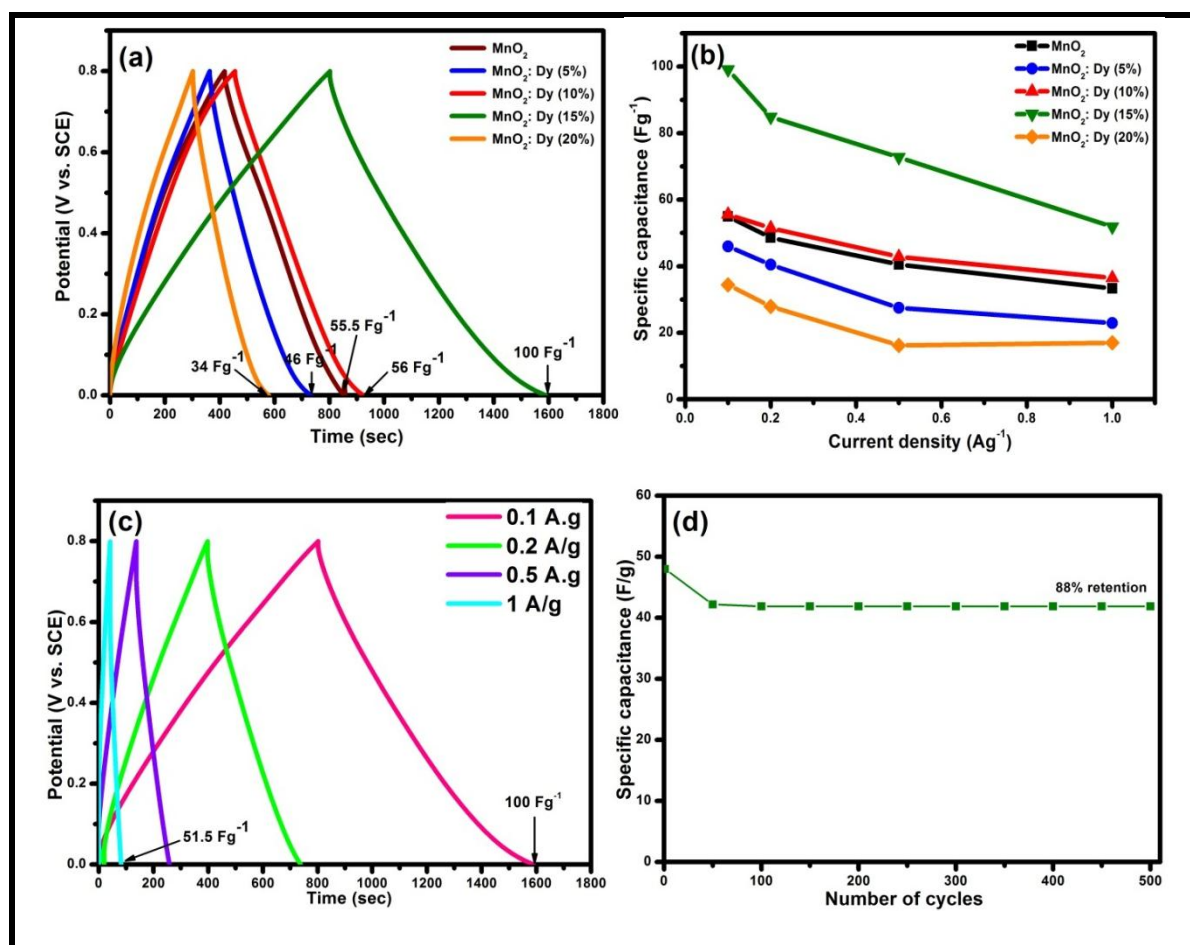
5.4.2 Galvanostatic Charge Discharge

Further, to check the charge storage capacity and stability of Dy doped α-MnO_2 electrode materials, charge / discharge (CD) measurement are carried out within the potential window of 0 to 0.8 V at various constant discharge current densities (0.1, 0.2, 0.5 and 1 Ag^{-1}) in 1M Na_2SO_4 aqueous electrolyte solution shown in Figure 5.9 (a). The linear and symmetric charge discharge profile of the potential with almost triangular shape reveals an excellent pseudocapacitive behaviour. The evaluation of the specific capacitance of electrodes from charge- discharge profiles has been done by using following equation:

$$Cp = \frac{I}{[m(\Delta v/\Delta t)]}$$ (5.2)

Table 5.3: Comparison of specific capacitance of metal oxides reported in literatures with the present material, α-MnO_2: Dy (15 mol %).

S.No.	Samples	Morphology	Specific capacitance	Current density (A/g)/ Scan rate (mV/sec)	Electrolyte	Reference
1.	**RuO₂/C**	Nanorods	151.3 F/g	5 mV/sec	1M H₂SO₄	(32)
2.	**α-Fe₂O₃**	Nanosheet	279.9 F/g	5 mV/sec	2M LiCl	(33)
3.	**TiO₂**	Nanofibers	65.84 F/g	1 mV/sec	1M KOH	(34)
4.	**SnO₂**	Nanoparticles	122 F/g	2 mV/sec	2M KOH	(35)
5.	**β-MnO₂**	Nanorods	125 F/g	1 A/g	3M KOH	(36)
6.	**0.125V-MnO₂**	Nanobelt	102 F/g	0.5 A/g	0.5 M Na₂SO₄	(37)
7.	**Ce doped α-MnO₂**	Nanorods	101.1 F/g	1 A/g	1M Li₂SO₄	(38)
8.	**α-MnO₂: Dy (15 mol %)**	Nanorods	111 F/g	5 mV/sec	1M Na₂SO₄	Present work

where, I is the constant discharge current (A), m is the mass (g) of the electrode material and $(\Delta v) / \Delta t$ is the slope of the chronopotentiometric discharge curve (Vsec^{-1}) [106]. Specific capacitance obtained for 0, 5, 10, 15 and 20 mol % of Dy in α-MnO$_2$ at constant discharge current density of 0.1 Ag^{-1} are 55, 46, 55.5, 100 and 34 Fg^{-1}, respectively.

***Figure 5.9:*** *(a) Galvanostatic charge discharge at 10 A/g, (b) specific capacitance at various current density of bare and α-MnO$_2$: Dy (5,10,15,20 mol%) nanorods, (c) charge discharge at different current densities and (d) cycling performance at the current density of 2 A/g of α-MnO$_2$: Dy (15 mol %).*

We observe that among all electrodes, α-MnO$_2$: Dy (15 mol %) shows highest capacitance (100 Fg^{-1}) as compared to bare α-MnO$_2$ (55 Fg^{-1}) which further reflects an improvement in electrochemical performance. Capacitance given by charge discharge profile is completely in consistent with the results obtained from CV measurements. It is clear that α-MnO$_2$: Dy (20 mol %) show a drop in capacitance which confirms that Dy ion can improve the specific capacitance of **α-MnO$_2$** electrode material upto certain doping concentration. Further, we have measured the capacitance at different current densities (0.1, 0.2, 0.5 and 1 Ag^{-1}) shown in Figure 5.9 (b). α-MnO$_2$: Dy (15 mol %) has a specific capacitance of 100 and 51.8 Fg^{-1} at a current density of 0.1 and 1 Ag^{-1}, respectively as illustrate in Figure 5.9 (c). Overall change in specific capacitance is 48.2%. We reveal the decay in specific capacitance with increasing current density. This decay in specific capacitance is because of the less involvement of active materials and exchange of electrons/ions between electrode and electrolyte. It is important to evaluate the capacitance retention over large number of cycles to investigate whether the electrode is suitable for practical application. The cyclic stability of α-MnO$_2$: Dy (15 mol %) electrode is determined by performing continuous charge/discharge over 500 cycles at a constant current density of 2 Ag^{-1}, as shown in Figure 5.9 (d). After being cycled for 500 cycles, α-MnO$_2$: Dy (15 mol %) electrode show 89% of capacitance retention from initial specific capacitance. The obtained result demonstrates the electrochemical stability of α-MnO$_2$: Dy (15 mol %) electrode material. These results suggest that doping Dy up to certain extent serve as an excellent electrode material and has a great potential application in future energy storage device.

5.4.3 Electrochemical Impedance Spectroscopy

We have further studied the mechanism of capacitance of bare and Dy doped MnO_2 electrodes by electrochemical impedance spectroscopy (EIS) within the frequency range of 10 kHz to 0.01 Hz in 1M Na_2SO_4 electrolyte solution at room temperature. A typical Nyquist plot for all the electrodes is shown in figure 5.10(a) consists of an incomplete semi-circular arc (inset of figure 5.9a) in high frequency region followed by a tail in low frequency one. The semi-circular arc indicates a pronounced pseudocapacitive behaviour. The impedance spectra of all the samples are analysed by ZsimpWin software on the basis of an electrical equivalent circuit, as displayed in the inset of figure 5.10 (a). The circuit consists of a solution resistance R_s, double layer capacitance C_{dl}, charge transfer resistance R_{ct} across electrode/electrolyte interface, low frequency resistance R_P corresponding to pseudocapacitor C_P. The straight line in low frequency region make an angle between 45° to 90° with the real impedance axis signifies that the process is governed by controlled diffusion of ions, fitted with Warburg element Z_w [133]. The fitted parameters of all the electrodes are tabulated in Table 5.4. In addition, from Bode plot the phase angle obtained for all electrodes reaches close to 80° reflects a typical pseudocapacitive behaviour shown in Figure 5.10 (b) [75][202]. The combination of Rs, R_{ct} and R_P gives the overall resistance of the electrodes which found to be low for α-MnO_2: Dy (15 mol %) in comparison to bare α-MnO_2. This implies that doping Dy ion increases the conductivity by reducing net resistance of α-MnO_2 electrode. The low frequency pseudocapacitance C_P gives the reliability of the fitted data which is in accordance with the values obtained from CV results.
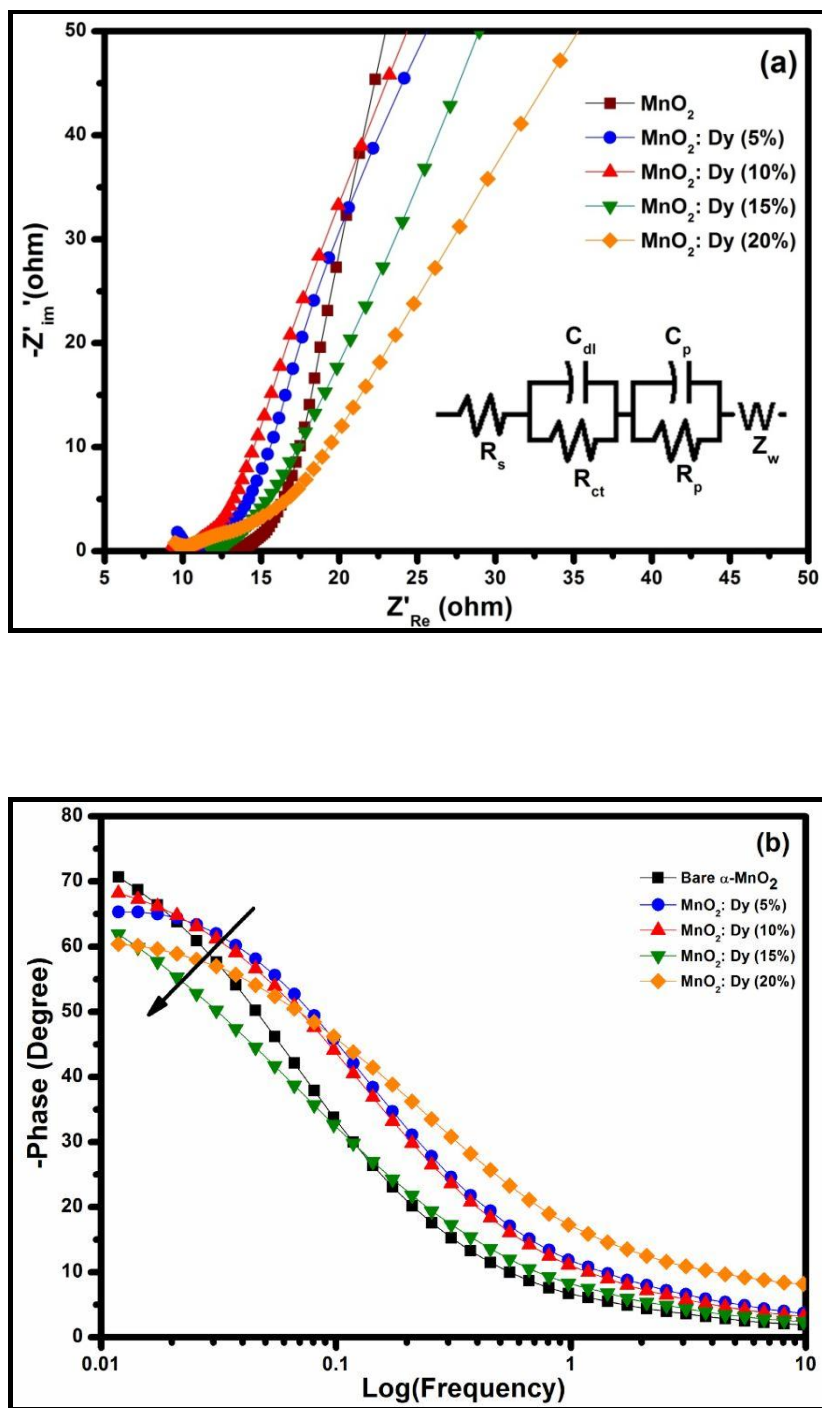
Figure 5.10: *(a) Nyquist plot showing charge transfer resistances and inset shows the electrical equivalent circuit for bare and α-MnO$_2$: Dy (5,10,15 & 20 mol%) nanorods and (b) Bode images of bare and α-MnO$_2$: Dy (5,10,15,20 mol%) nanorods.*

Table 5.4: EIS fitted parameters of bare MnO_2 and α-MnO_2: Dy (5, 10, 15 and 20 mol %).

Sr. No.	R_s (Ω)	R_{ct} (Ω)	C_{dl} (mF)	R_L (kΩ)	C_p (F/g)	Zw (Ω)
α-MnO_2	12.17	1.244	0.038	3.648	15.80	0.1226
α-MnO_2: Dy (5 mol %)	9.834	1.575	0.015	0.781	15.90	0.07642
α-MnO_2: Dy (10 mol %)	9.131	0.9468	0.043	0.630	60.06	0.1571
α-MnO_2: Dy (15 mol %)	9.537	1.866	0.021	0.438	51.45	0.07891
α-MnO_2: Dy (20 mol %)	7.473	1.27	0.076	1.370	24.87	0.01473

5.5 Conclusion

Tetragonal, I4/m structure of α-MnO_2 nanorods with different concentration of Dy were synthesised via simple one step hydrothermal method without using any template. Incorporation of Dy ion not only influenced the crystalline nature but also inhibited the growth of nanorods. With increasing Dy concentration in α-MnO_2 although, the structure of MnO_2 remained tetragonal, the crystallinity deteriorated and inhibited the growth rate of nanorods. We observed that when the concentration of Dy reached 15 mol%, the diameter and length of α-MnO_2 nanorods reduced from 40 nm and 4-5 µm to 20 nm and 70 nm, respectively. Being MnO_2 as a good electroactive material, a significant enhancement in specific capacitance accompanied with a decrease in charge transfer resistance after incorporating 15 mol% Dy was observed. Such enhancement in specific capacitance attributed to poor crystallinity along with large surface area and pore size distribution. Here we concluded that rare earth doped α-MnO_2 can be explored as an eminent electrode material for an application of supercapacitor.

Chapter 6 *Magnetic Properties of Dy Doped α-MnO$_2$ Nanorods*

6.1 Introduction

In previous chapter, we have demonstrated the effect of doping of dysprosium on α-MnO$_2$ nanorods and its effect on structural and electrochemical properties. We observed that 15% of Dy doped in α-MnO$_2$ nanorods possess high specific capacitance and can be used as an electrode in supercapacitors. In addition to its electrochemical characteristics, the magnetic properties are also interesting to study in these samples as there are rare report on the magnetic properties of rare earth doped α-MnO$_2$. Therefore, in this chapter, we have explained the evolution of magnetic properties of bare and 15 mol % Dy-doped MnO$_2$ nanorods synthesised using simple one step hydrothermal process. As structural modifications are already explained in the previous chapter, here the oxidation states are determined by X-ray photoelectron spectroscopy and illustrated in section 6.2. Magnetic properties are examined using temperature dependent magnetization, field dependent magnetization and remanant magnetization, as discussed in section 6.3. We observe a decrease in Neel temperature with an increase in Curie-Weiss temperature after doping Dy in α-MnO$_2$ nanorods indicating strong antiferromagnetic interaction. We measure exchange bias and training effect and have discussed on the basis of phenomenological models. The variation in exchange bias of both samples has been explained on the basis of core shell model and concluded in section 6.4.